nature geoscience

ARTICLES

https://doi.org/10.1038/s41561-019-0405-8

Corrected: Author Correction

Thick ice deposits in shallow simple craters on the Moon and Mercury

Lior Rubanenko*, Jaahnavee Venkatraman and David A. Paige

Permanently shadowed regions near the poles of Mercury and the Moon may cold-trap water ice for geologic time periods. In past studies, thick ice deposits have been detected on Mercury, but not on the Moon, despite their similar thermal environments. Here we report evidence for thick ice deposits inside permanently shadowed simple craters on both Mercury and the Moon. We measure the depth/diameter ratio of approximately 2,000 simple craters near the north pole of Mercury using Mercury Laser Altimeter data. We find that these craters become distinctly shallower at higher latitudes, where ice is known to have accumulated on their floors. This shallowing corresponds to a maximum infill of around 50 m, consistent with previous estimates. A parallel investigation of approximately 12,000 lunar craters using Lunar Reconnaissance Orbiter data reveals a similar morphological trend near the south pole of the Moon, which we conclude is also due to the presence of thick ice deposits. We find that previously detected surface ice deposits in the south polar region of the Moon are spatially correlated with shallow craters, indicating that the surface ice may be exhumed or linked to the subsurface via diffusion. The family of lunar craters that we identify are promising targets for future missions, and may also help resolve the apparent discrepancy between the abundance of frozen volatiles on Mercury and the Moon.

The origins and distribution of cold-trapped ices near the poles of Mercury and the Moon are poorly constrained. The low obliquity of these planetary bodies causes polar topographic depressions to cast highly persistent shadows[1]. If sufficiently cold, these permanently shadowed regions (PSRs) are able to trap and preserve volatiles, such as water ice, for billions of years[2]. Evidence gathered by the Arecibo radio telescope and later by the Mercury Surface, Space Environment, Geochemistry and Ranging (MESSENGER) spacecraft indicates that cold-traps on Mercury harbour pure ice deposits more than a few metres thick[3–6]. Similar radar investigations conducted on the Moon have thus far found little evidence for widespread thick ice deposits[7,8]. The Lunar Crater Observation and Sensing Satellite (LCROSS) mission detected 5%–10% water by mass[9] in the uppermost few metres of the floor of Cabeus Crater. Thus far, only scattered surface and near-surface deposits have been detected in polar cold-traps by the Lunar Reconnaissance Orbiter (LRO)[10–12]. This difference is particularly surprising as the polar thermal environments and the net volatile accumulation rates on Mercury and the Moon are not believed to be vastly different[5,13,14]. Adding to the puzzle, neutron spectrometers have detected enhanced hydrogen concentrations in the near subsurface of both Mercury and the Moon that are probably due to the presence of water ice[15–17].

Here we analyse the morphology of 2.5–15 km craters near the north pole of Mercury and find that they contain thick ice deposits, congruous with earlier observations of thick ice in larger craters. By performing a similar analysis on the Moon, we infer the existence of analogous thick ice deposits in shallow craters near the lunar south pole.

Evidence for ice in craters on Mercury and the Moon

We identify 2,069 simple craters (diameter 2.5–15 km) on the Mercury Dual Imaging System (MDIS[18]) basemap and measure their depth/diameter (d/D) ratios using the Mercury Laser Altimeter (MLA[19]) polar topographic basemap gridded at a resolution of 250 m px^{-1} (Fig. 1a; see Methods). We restrict our measurements to latitudes >75°–88° N, where the highest quality MLA and MDIS data were gathered due to MESSENGER's orbit. Figure 1b shows that the mean d/D ratio of all craters decreases by ~10% from latitude 75° to 86°. Extrapolating this trend to the pole yields a maximal shallowing of ~20% (roughly 50 ± 5 m), considering our crater size range (see Supplementary Information for error estimation). In lower latitudes, the smaller permanently shadowed volume cast by craters restricts the amount of ice they may potentially trap. The average infill, therefore, is lower: ~15 ± 1 m. Results are shown in Fig. 1. The grey dots in the lower panels represent craters that cast permanent shadows, as calculated using an analytic shadowing model. The blue dots are craters that both cast permanent shadows and are also sufficiently cold to trap water ice according to an analytic radiation scattering model[20]. The black dashed lines show the extent to which these craters are filled relative to their potential ice filling capacity that is, to first order, given by the volume of the PSR they cast[21] (see Methods).

The poleward shallowing we observe on Mercury is consistent with the presence of previously detected thick water ice deposits in larger craters. We support this claim by several lines of evidence. First, the mean d/D decreases at the same latitudes in which craters are modelled to cold-trap significant amounts of water ice (Fig. 1a, see Methods). We note the shallowing does not fit the presence of other prevalent volatile species, as those are cold-trapped at different temperatures[5,21].Second, as ice accumulates in cold-traps, it should have a greater effect on the depth of smaller craters compared to larger craters. We find that the shallowing trend in larger craters, 7.5–15 km, is significantly diminished compared to smaller craters, 2.5–5 km (Supplementary Fig. 1). Third, the colder pole-facing slopes of atypically shallow craters are shallower than the warmer, equator-facing slopes (Supplementary Fig. 2). On Mercury, the median of the pole-facing slopes distribution is ~10% shallower than that of the equator-facing slopes distribution. Fourth, the average shallowing we measure corresponds to approximately

Department of Earth, Planetary and Space Sciences, University of California, Los Angeles, CA, USA. *e-mail: liorr@ucla.edu

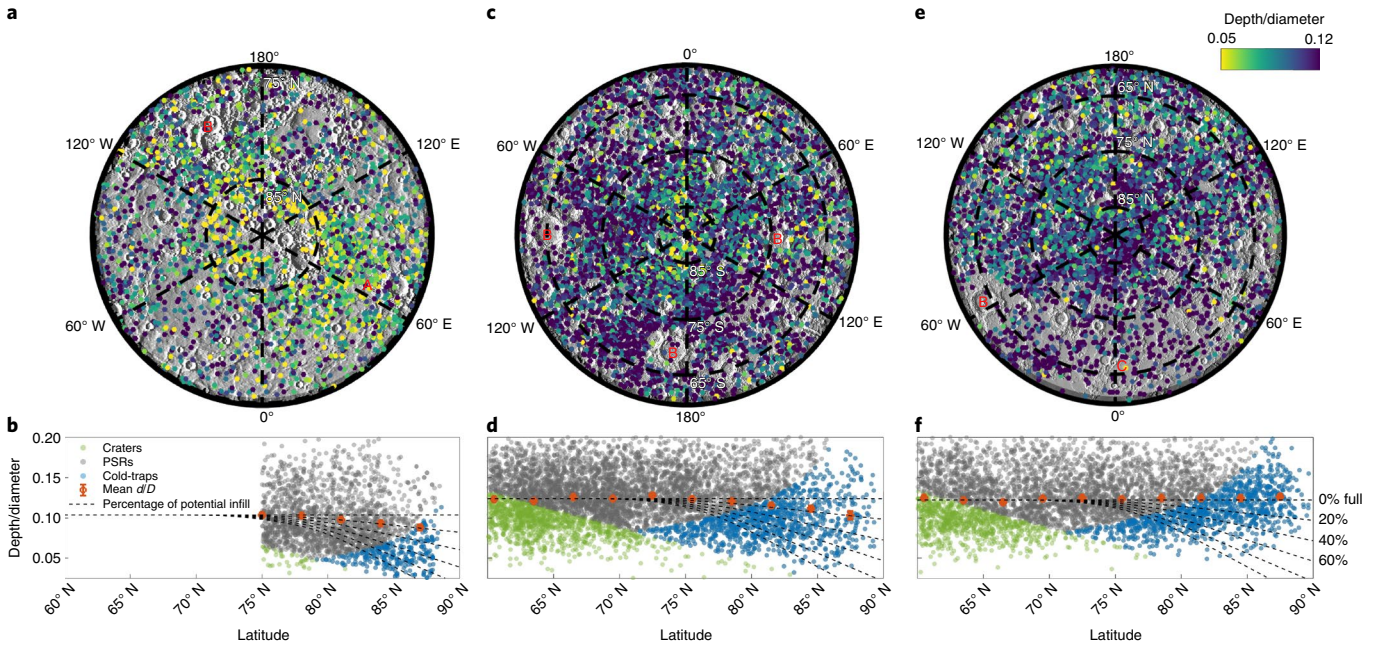

Fig. 1 | Shallow craters near the poles of Mercury and the Moon. a,**c**,**e**, Maps showing the catalogued craters with their corresponding *d*/*D* ratios for Mercury's north pole (**a**) (latitude >75° N), and the Moon's south (**c**) and north poles (**f**) (latitude >60° N/S). The red uppercase letters indicate areas of interest. A: large population of shallow, elliptical craters that are possibly secondary craters of Prokofiev Crater. B: the lower crater density near larger craters (for example, lunar Antoniadi, Hausen and Pythagoras Craters, all Upper Imbrian[33,34]) indicates that our sampled smaller craters are typically a few billion years old. C: the crater density is much lower in and around the lunar Maria. **b**,**d**,**f**, Plots showing the *d*/*D* ratios of all the craters sampled for Mercury's north pole (**b**), and the Moon's south (**d**) and north (**f**) poles. The green and grey markers are non-permanently and permanently shadowed craters, respectively. The blue markers indicate craters that are sufficiently cold to trap water ice according to a thermal model[20]. The red markers show the mean *d*/*D* ratio of all the catalogued craters in bins of 3°, after removing craters suspected as secondaries (see Methods). The black dashed lines show the extent to which craters are filled relative to their potential ice filling capacity based on PSV. The error bars indicate one standard error to the mean.

20% of the permanent shadow volume (PSV), or roughly 10 m, in accord with previous theoretical[22] and observational[6] estimates for the thickness of polar ice deposits detected in individual craters[3–5,23]. Our statistical approach allows us to better constrain the average thickness of polar ice deposits than has been possible in previous studies. Fifth, Mercury's eccentric orbit and its 3:2 spin–orbit resonance causes roughly half its polar region (termed 'the warm pole' longitudes) to be exposed to more insolation than the other half (termed 'the cold pole' longitudes)[24]. We find that craters in the cold pole longitudes of Mercury are shallower than craters in its warm pole longitudes (Supplementary Fig. 3).

We have conducted a parallel investigation of the morphology of simple craters in the polar regions on the Moon. The polar orbit of LRO allows us to extend our survey to latitudes 60°–90° (N/S) and measure 11,228 craters in the same size range as on Mercury (Fig. 1c–f; see Methods). We refine the data as explained above and in the Methods. Figure 1d,f shows that the *d*/*D* ratio of lunar craters decreases with latitude near the south pole but not the north pole of the Moon. We note that in both polar regions, the average *d*/*D* equatorward of latitude 75° N/S is nearly equal and matches previous surveys[25], 0.1242 and 0.1262 for the northern and southern hemispheres, respectively. In the southern hemisphere, the shallowing starts near latitude 75° S, where craters become cold-traps according to thermal models[20,26], and extends to the pole. Near the south pole, craters become ~15% shallower, corresponding to a maximal shallowing of ~50 ± 4 m. The average infill is ~10 ± 1 m. A previous study[27] documented similar crater shallowing at both lunar poles for a smaller sample size and smaller crater size range, finding south polar craters to be shallower than north polar craters.

The morphological trend we observe near the south pole of the Moon resembles the one on Mercury; the poleward shallowing is of the same order (Fig. 1b), and pole-facing slopes are slightly shallower than the equator-facing slopes (Supplementary Fig. 2b). This resemblance, along with the correlation we find between cold-trapping craters and their *d*/*D*, leads us to conclude that craters become shallower due to the presence of thick ice deposits (Fig. 1). The absence of an analogous morphological trend near the north pole does not necessarily imply a null result; ice deposits may still be present in north polar craters, but the deposits may not be sufficiently thick to cause statistically significant shallowing.

Nature of trapped ice deposits

Next we examine the relationship between the thick ice deposits we infer in this study and previously detected surface ice on the Moon, obtained by correlating near-infrared spectroscopy acquired by the Moon Mineralogy Mapper (M^3) on Chandrayaan-1 with data acquired by LRO[12]. We divide each polar region (latitudes 80–90 N/S) into areal bins of 60 km^2, and calculate the mean *d*/*D* and surface ice area fraction in every bin (see Methods). Figure 2 shows that the mean *d*/*D* is negatively correlated with the surface ice area fraction in the south pole, suggesting that some of these surface ice deposits may be exhumed or replenished by water molecules diffusing from depth, a process that has been demonstrated theoretically to be possible on geologic timescales[28,29]. However, this correlation does not rule out other mechanisms for the present-day accumulation of surface ice, such as the cold-trapping of exospheric volatiles[2,30].

In the north polar region of the Moon we find that shallow craters are not spatially correlated with the locations of surface ice

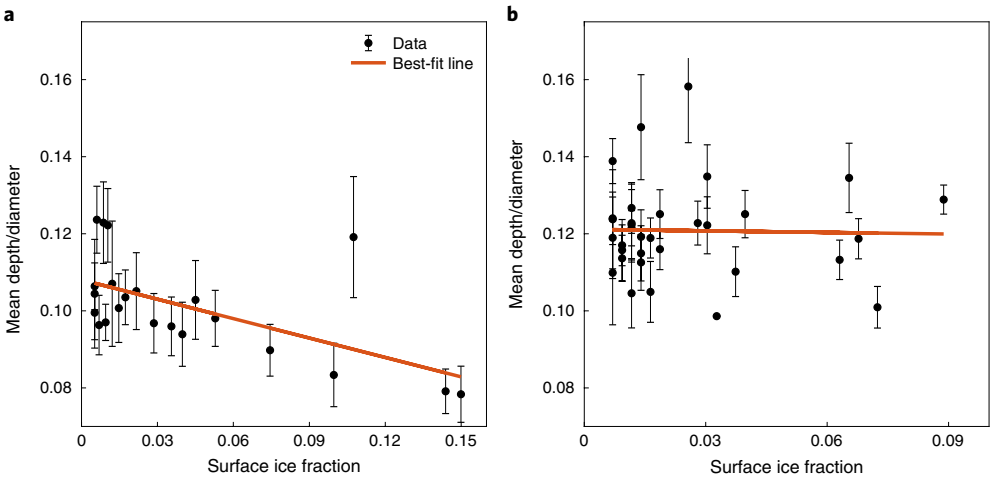

Fig. 2 | Sparse surface ice deposits previously identified on the Moon are negatively correlated with craters' *d/D*. Surface ice data were composed by correlating near-infrared spectra obtained by M^3 aboard the Chandrayaan-1 with data acquired by LRO[12]. **a**,**b**, We find a negative spatial correlation between the family of shallow craters we identified near the south pole (**a**) but not near the north pole (**b**) of the Moon. For clarity, we show only bins with surface ice fraction >0.5%. Craters under that threshold do not significantly affect our result, emphasized by the least-squares best-fit line. The error bars represent one standard error to the mean. Some of the error bars are smaller than the data points they support.

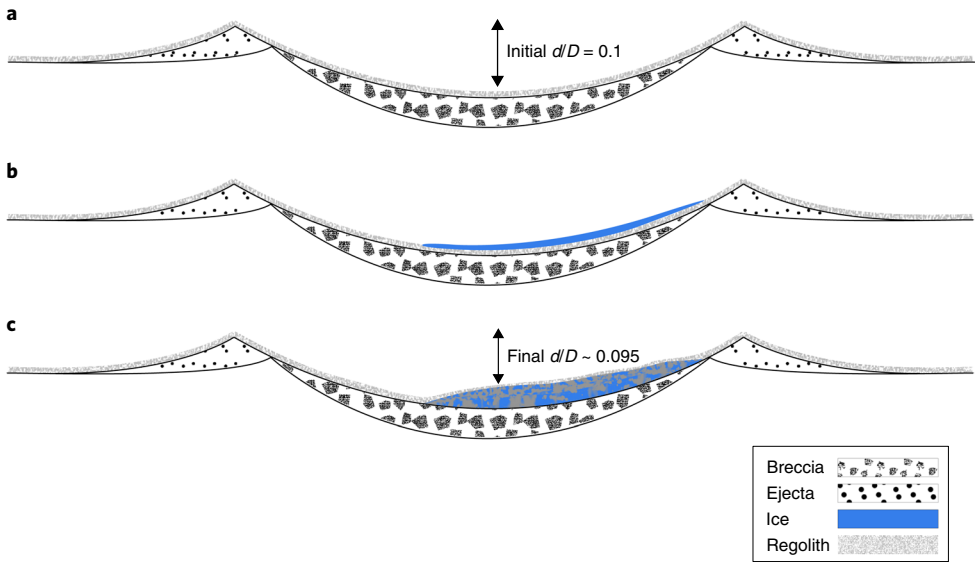

Fig. 3 | Ice accumulation, burial and gardening in an impact crater with a diameter of 3 km and *d/D* of 0.1. a, A crater is formed, and then covered by regolith. **b**, A ~10-m-thick ice deposit accumulates in the crater over a short time period. **c**, Ejecta from nearby craters or mass wasting buries the ice, slowing sublimation. With time, impact gardening exposes some of the ice, or it may reach the surface by way of diffusion. This process may repeat itself after each deposition. The vertical dimension is exaggerated for emphasis.

deposits. The lack of this correlation in the north, along with the absence of a morphological trend mirroring the one in the south, is puzzling and poorly understood. A possible explanation may lie in the relative ease of volatile destruction compared to volatile accumulation. It is possible that craters in the north contained thick ice deposits in the past that were later destroyed by, for example, the heat produced by the Imbrium-forming impact (see Supplementary Information). This is consistent with the previously observed sparsity of surface ice in the north relative to the south[11,12].

Considering the ~10 m average shallowing we infer for lunar south polar craters and assuming a typical ice-free lunar highlands regolith thickness of ~10–20 m (ref. [31]), we estimate that lunar subsurface deposits may be typically composed of ~30–50% ice by mass. Water ice in these concentrations would not be expected to produce strong radar backscattering, which is in general agreement with available lunar radar observations[7,8,32]. These ice concentrations are also in rough agreement with the results of the LCROSS impact in Cabeus Crater, which have been interpreted to indicate the presence of up to 10% ice by mass in the uppermost metres[9].

Ice accumulation history on Mercury and the Moon

The areal density of craters in our survey is depressed in the areas surrounding larger Upper Imbrian craters such as Antoniadi, Hausen and Pythagoras (Fig. 1, regions marked B). This indicates that the smaller craters in our sample predate these Upper Imbrian craters—and thus are typically a few billion years old[33,34]. Although

the age of the craters puts an upper limit on the age of the deposits, it does not preclude the possibility that they may be due to a recent asteroid or comet impact. However, we find it more likely that these deposits are primordial due to their thickness, which implies that they were delivered over long timescales, and the absence of a clear radar signal, which implies that they are buried or mixed into the regolith.

A potential mechanism for the accumulation of buried, eroded water ice deposits in craters is shown in Fig. 3. Surface ice accumulates equally in all permanently shadowed craters due to, for example, a large comet impact. After ice is deposited into cold-traps, it is buried under regolith ejected by mass wasting or from nearby impact craters (Fig. 3a,b). Finally, the regolith is gardened and the ice is exposed, producing a deposit with a low ice fraction at the surface. This process may repeat itself. In this model, polar ice deposits have a distinct topographic signature that is more readily detected in smaller craters because of their relative larger infill. However, these physical mechanisms we propose to be responsible for the accumulation and burial of ice should operate equally well in larger cold-traps to create ~10-m-thick ice-rich layers.

Future investigations of polar deposits

The statistical methodology employed in our study prevents us from identifying specific craters that contain ice, as individual craters may appear shallower or deeper than average due to their impact formation energy or the local geology[35]. We find it unlikely that phenomena unrelated to volatiles such as contamination by secondary craters, a local geologic deposit with different material strength, or crater degradation cause the shallowing we observe. Removing highly elliptical craters, suspected as secondaries, does not significantly affect our results. Furthermore, we find no correlation between craters' d/D and the presence of large geologic deposits or the age of the surface (see full discussion in Supplementary Information).

We may use our results to re-estimate the total mass of the ice trapped in the lunar poles. Lunar cold-traps have been previously estimated to occupy ~10^4 km^2 (ref. [13]). If all cold-traps hide a ~10-m-thick pure subsurface ice deposit, the total mass of water ice on the Moon could be estimated to be up to ~100 billion metric tons. This is approximately two orders of magnitude greater than previous estimates that are based on surface detections and the LCROSS impact results[9,10–12]. Our results combined with previous radar data imply that the most concentrated lunar ice deposits are likely to be buried a few meters under permanently shadowed south polar cold-traps. The possibility that thick ice-rich deposits exist on the Moon may not only help resolve the outstanding question regarding its low ice abundance relative to Mercury, but may also have practical applications in preparation for a future permanent lunar settlement.

Online content

Any methods, additional references, Nature Research reporting summaries, source data, statements of code and data availability and associated accession codes are available at https://doi.org/10.1038/s41561-019-0405-8.

Received: 6 December 2018; Accepted: 11 June 2019;
Published online: 22 July 2019

References

1. Urey, H. C. *The Planets, Their Origin and Development* (Yale Univ. Press, 1952).
2. Watson, K., Murray, B. & Brown, H. On the possible presence of ice on the Moon. *J. Geophys. Res.* **66**, 1598–1600 (1961).
3. Harmon, J. K. & Slade, M. A. Radar mapping of mercury: full-disk images and polar anomalies. *Science* **258**, 640–643 (1992).
4. Slade, M. A., Butler, B. J. & Muhleman, D. O. Mercury radar imaging: evidence for polar ice. *Science* **258**, 635–640 (1992).
5. Paige, D. A. et al. Thermal stability of volatiles in the north polar region of Mercury. *Science* **339**, 300–303 (2013).
6. Deutsch, A. N., Head, J. W., Chabot, N. L. & Neumann, G. A. Constraining the thickness of polar ice deposits on Mercury using the Mercury Laser Altimeter and small craters in permanently shadowed regions. *Icarus* **305**, 139–148 (2018).
7. Stacy, N. J. S., Ford, P. G. & Campbell, D. B. Arecibo radar mapping of the lunar poles: a search for ice deposits. *Science* **276**, 1527–1530 (1997).
8. Campbell, D. B., Campbell, B. A., Carter, L. M., Margot, J.-L. & Stacy, N. J. S. No evidence for thick deposits of ice at the lunar south pole. *Nature* **443**, 835–837 (2006).
9. Colaprete, A. et al. Detection of water in the LCROSS ejecta plume. *Science* **330**, 463–468 (2010).
10. Hayne, P. O. et al. Evidence for exposed water ice in the Moon's south polar regions from Lunar Reconnaissance Orbiter ultraviolet albedo and temperature measurements. *Icarus* **255**, 58–69 (2015).
11. Fisher, E. A. et al. Evidence for surface water ice in the lunar polar regions using reflectance measurements from the Lunar Orbiter Laser Altimeter and temperature measurements from the Diviner Lunar Radiometer Experiment. *Icarus* **292**, 74–85 (2017).
12. Li, S. et al. Direct evidence of surface exposed water ice in the lunar polar regions. *Proc. Natl Acad. Sci. USA* **115**, 8907–8912 (2018).
13. Paige, D. A. et al. Diviner Lunar Radiometer observations of cold traps in the Moon's south polar region. *Science* **330**, 479–482 (2010).
14. Lawrence, D. J. A tale of two poles: Toward understanding the presence, distribution, and origin of volatiles at the polar regions of the Moon and Mercury. *J. Geophys. Res. Planets* **122**, 21–52 (2017).
15. Mitrofanov, I. G. et al. Hydrogen mapping of the lunar south pole using the LRO neutron detector experiment LEND. *Science* **330**, 483–486 (2010).
16. Feldman, W. C. et al. Fluxes of fast and epithermal neutrons from Lunar Prospector: evidence for water ice at the lunar poles. *Science* **281**, 1496–1500 (1998).
17. Lawrence, D. J. et al. Evidence for water ice near Mercury's north pole from MESSENGER Neutron Spectrometer measurements. *Science* **339**, 292–296 (2013).
18. Hawkins, S. E. et al. The Mercury dual imaging system on the MESSENGER spacecraft. *Space Sci. Rev.* **131**, 247–338 (2007).
19. Cavanaugh, J. F. et al. The Mercury Laser Altimeter Instrument for the MESSENGER Mission. *Space Sci. Rev.* **131**, 451–479 (2007).
20. Ingersoll, A. P., Svitek, T. & Murray, B. C. Stability of polar frosts in spherical bowl-shaped craters on the Moon, Mercury, and Mars. *Icarus* **100**, 40–47 (1992).
21. Rubanenko, L., Mazarico, E., Neumann, G. A. & Paige, D. A. Ice in Micro Cold Traps on Mercury: Implications for Age and Origin. *J. Geophys. Res. Planets* **123**, 2178–2191 (2018).
22. Moses, J. I., Rawlins, K., Zahnle, K. & Dones, L. External sources of water for Mercury's putative ice deposits. *Icarus* **137**, 197–221 (1999).
23. Chabot, N. L. et al. Images of surface volatiles in Mercury's polar craters acquired by the MESSENGER spacecraft. *Geology* **42**, 1051–1054 (2014).
24. Paige, D. A., Wood, S. E. & Vasavada, A. R. The thermal stability of water ice at the poles of mercury. *Science* **258**, 643–646 (1992).
25. Salamunićcar, G., Lončarić, S., Grumpe, A. & Wöhler, C. Hybrid method for crater detection based on topography reconstruction from optical images and the new LU78287GT catalogue of Lunar impact craters. *Adv. Space Res.* **53**, 1783–1797 (2014).
26. Rubanenko, L. & Aharonson, O. Stability of ice on the Moon with rough topography. *Icarus* **296**, 99–109 (2017).
27. Kokhanov, A. A., Kreslavsky, M. A. & Karachevtseva, I. P. Small impact craters in the polar regions of the Moon: peculiarities of morphometric characteristics. *Sol. Syst. Res.* **49**, 295–302 (2015).
28. Schorghofer, N. & Taylor, G. J. Subsurface migration of H_2O at lunar cold traps. *J. Geophys. Res. Planets* **112**, E02010 (2007).
29. Schorghofer, N. & Aharonson, O. The lunar thermal ice pump. *Astrophys. J.* **788**, 169 (2014).
30. Schorghofer, N. Two-dimensional description of surface-bounded exospheres with application to the migration of water molecules on the Moon. *Phys. Rev. E* **91**, 052154 (2015).
31. Fa, W. & Wieczorek, M. A. Regolith thickness over the lunar nearside: results from Earth-based 70-cm Arecibo radar observations. *Icarus* **218**, 771–787 (2012).
32. Spudis, P. D. et al. Evidence for water ice on the Moon: results for anomalous polar craters from the LRO Mini-RF imaging radar. *J. Geophys. Res. Planets* **118**, 2016–2029 (2013).
33. Haruyama, J. et al. Long-lived volcanism on the lunar farside revealed by SELENE terrain camera. *Science* **323**, 905–908 (2009).
34. McEwen, A. S. et al. Galileo observations of post-Imbrium lunar craters during the first Earth–Moon flyby. *J. Geophys. Res. Planets* **98**, 17207–17231 (1993).
35. Pike, R. J. in *Impact and Explosion Cratering* (eds Roddy, D. J. et al.) 489–509 (Pergamon, 1977).

Acknowledgements

This work was supported in part by the Lunar Reconnaissance Orbiter Diviner (award no. NNG09EK06C) and MESSENGER (grant no. NNX07AR64G) missions. We are grateful to J.-P. Williams for helpful discussions and suggestions and S. Li for providing us with his previously published surface ice data. L.R. thanks T. Powell for many helpful discussions. The authors would also like to express their gratitude to the LOLA and MLA teams for acquiring high-precision laser altimeter datasets of the Moon and Mercury. LRO and MLA data were obtained from the Planetary Data System.

Author contributions

L.R. proposed the idea, and collected and analysed the majority of the data. J.V. assisted in identifying and measuring craters. L.R. interpreted the data and wrote the manuscript along with D.A.P.

Competing interests

The authors declare no competing interests.

Additional information

Supplementary information is available for this paper at https://doi.org/10.1038/s41561-019-0405-8.

Reprints and permissions information is available at www.nature.com/reprints.

Correspondence and requests for materials should be addressed to L.R.

Publisher's note: Springer Nature remains neutral with regard to jurisdictional claims in published maps and institutional affiliations.

Methods

Identifying and measuring craters. We begin by manually identifying simple impact craters on the MDIS and LRO Camera (LROC) visible imagery polar mosaics using the JMARS crater counting tool. We record the crater coordinates and diameter, omitting craters that overlap other craters as those might not have a symmetric profile. In lower latitudes, the lighting conditions might make it more difficult to identify shallower craters. To mitigate this observation bias, we use the shaded relief polar mosaics calculated by the Lunar Orbiter Laser Altimeter (LOLA), LROC and MLA as an additional reference. For MLA and LOLA, we have used data obtained from Planetary Data System 3, v.2 (refs. [36,37]). After identifying the craters, we extract three topographic profiles from the MLA and LOLA elevation maps gridded at a resolution of 250 m px^{-1} and 120 m px^{-1}, respectively. One profile in the equatorial–polar direction, and two additional profiles along the long and short axes of the crater. We choose the craters' long and short axes from 50 topographic profiles passing through the center of the crater and rotated at a fixed angular increment. To measure the crater's depth, diameter and mean slope we find the crater's rims and centre using an algorithm we developed: we begin by subtracting a linear least-squares best fit from the profile to remove large-scale slope effects. Then, we smooth the topography using a Gaussian filter to remove small-scale topographic noise. We calculate the second derivative of the profile to find the deepest point in the crater. Using this point as a reference, we divide the crater into two parts. For each part, we calculate the first derivative and set the rim as the location in which it decreases to 10% of the steepest slope. The horizontal coordinate of the centre of the crater is defined as the median of the line segment bounded between the two rims. The depth of the crater is calculated as the difference between the average height of the rims and the height of its centre averaged over the three profiles. The diameter of the crater is set as the distance between the two rims. The median profile slope used to derive Supplementary Fig. 3 is calculated as the median of the first derivative of the polar–equatorial profile of the craters in our sample. The data are further processed by manually reviewing the topographic profiles and discarding false positives. We remove outliers ($d/D < 0.025$ and $d/D > 0.25$), and those suspected as secondaries that may skew our results (see later). The contours in Supplementary Fig. 8 outline the full extent of the data range in depth–diameter space. Our catalogue is complete to a d/D of ~0.07 relative to a recently acquired lunar crater catalogue[25].

Removing secondary craters. Secondary craters tend to be shallower and more elliptical than primary craters[38]. Consequently, a recent prominent polar impact (such as the one that formed Prokofiev Crater) might skew our result by contaminating the polar region with secondaries, lowering its mean crater depth. We deal with this possible contamination by discarding highly elliptic craters (circularity <0.85, characteristic limit for secondaries[39]) and those found along crater rays. In this process, we have removed ~10–15% of the overall crater population. For example, and although this is not in the scope of this work, we identify and map craters suspected as Prokofiev Crater's secondaries (group A in Fig. 1a). These craters are anomalously shallow and elliptic, and follow distinct crater rays that stretch from Prokofiev Crater towards the equator.

Maximum potential ice infill and cold-trapping ability. To first order, the thickness of a cold-trapped ice deposit is limited by the depth of the PSV harbouring it[21]. We use this limit to estimate to what extent the depth of a simple crater would change due to the presence of a thick ice deposit. Simple craters <15 km are well approximated by hemispherical (bowl-shaped) cavities[20,40,41]. This approximation allows calculating the PSV and cold-trapping ability of craters as a function of latitude and d/D ratio. To prepare Fig. 1d–f we determine which craters in our sample would cast permanent shadows (grey dots) and which will not (green dots). The deepest instantaneous shadow d_s cast by a crater with depth d at incidence angle θ_i is

$$\frac{d_s}{d} = \beta - \sin\theta_i\left(\beta - 1 + \cot\theta_i\sqrt{2\beta - 1}\right) \quad (1)$$

where $\beta \equiv \frac{1+4\Delta^2}{8\Delta^2}$, and Δ is the crater d/D ratio. Craters will cease casting a permanent shadow for $d_s = 0$, which occurs when

$$\beta = \frac{1}{1-\sin\theta_i}$$

Assuming the obliquity is very small, at noon the incidence angle equals the local latitude, $\varphi = \theta_i$, and the above equation can be reduced to

$$\sin\varphi = \frac{1-4\Delta^2}{1+4\Delta^2} \quad (2)$$

The shallowest instantaneous shadow cast at the centre of the crater during the day sets the depth of the permanent shadow at the same point. For hemispherical craters, this shallowest instantaneous shadow is cast at noon, when the solar incidence angle equals the local latitude. The maximum potential ice infill is the extent to which an ice deposit would decrease the depth of a simple crater. As explained above, the PSV depth is an upper limit for this maximum potential ice infill. We can calculate the depth of the PSV at the centre of the crater using simple trigonometry

$$\frac{d_s}{d} = 1 - \frac{1}{2\Delta}\cot\theta_i \quad (3)$$

We use this equation to plot the black contours shown in Fig. 1d–f.

Our simplified permanent shadow model assumes that regional slopes do not tilt the crater and that the obliquity, and thus the solar declination angle, is zero. In addition, it assumes an idealized hemispherical shape for the crater and ignores small-scale topographic imperfections such as impact craters and mass wasting. The former are factors that may potentially impair the ability of the crater to cast a permanent shadow: tilted surfaces may expose the floor of the crater to solar illumination at angles not predicted by our model, and the obliquity to the ecliptic causes the Sun to be slightly higher at noon and rise and set at different solar azimuths throughout the year. The latter is a more important effect that may be analytically quantified. The azimuth of sunrise/sunset is given by

$$\cos a_s = \frac{\sin\delta}{\cos\phi} \quad (4)$$

where δ is the solar declination angle and ϕ is the latitude. Taking the largest solar declination δ = obliquity, as is the case at summer solstice, we see that the effect of obliquity on the permanent shadow is greatest in high latitudes. For example, the lunar obliquity is ~1.5°; in latitude 80°, the largest deviation in azimuth of the sunrise from east is ~9° towards the pole. However, this effect is compensated for by the low maximum possible solar elevation angle that leaves most of the crater's floor shadowed.

Determining ice stability in craters. Ice stability on airless surfaces is proportional to the equilibrium vapour pressure. Consequently, it is highly sensitive to temperature variations[2,28]. For example, the sublimation rate of exposed ice at 115 K is ~1 m per billion years, three orders of magnitude greater than the sublimation rate 100 K. Consequently, it is common to define a 'cold-trap temperature', above which volatiles cannot remain stable for geologic time periods. This definition varies as it depends on the mass of the sublimating ice deposit and the timescales. Here we choose this temperature to be $T_{ct} = 115$ K, corresponding to a sublimation rate of ~1 m per billion years appropriate for our problem. The temperature distribution of a hemispherical (bowl-shaped) crater depends on the regolith optical properties, the crater latitude and the d/D ratio Δ. To estimate which craters are cold-traps, we calculate their PSR equilibrium temperature T using an analytic scattering model[20,41]

$$\sigma T^4 = F_0 \sin e_0 \frac{f - Af}{1 - Af}\left[1 + \frac{A(1-f)}{\varepsilon}\right] \quad (5)$$

where F_0 is the solar constant, e_0 is the solar elevation angle, A is the surface albedo, $\varepsilon = 0.95$ (ref. [26]) is the infrared emissivity and $f = 1/(1 + 1/4\Delta^2)$. For Mercury, we use $A = 0.08$ and for the Moon $A = 0.13$ (refs. [21,42]). The highest PSR temperature during the day, which serves as the criterion for ice stability, is obtained at noon, when the solar elevation angle equals the co-latitude. To find which craters are cold-traps, we first determine which craters cast a permanent shadow using equation (2), and then verify that this shadow temperature is lower than T_{ct} using equation (4).

Correlation between surface ice and crater morphology. Recently[10–12], positive detections of surface ice deposits were mapped by constraining near-infrared spectra obtained by the M^3 instrument onboard the Chandrayaan 1 spacecraft with previously gathered LRO data[10–12]. To test whether these detected surface ice deposits are spatially correlated with the family of shallow craters we identify here, we divide the polar region (between 80° N/S and the pole) into areal bins of 60 km^2. For each bin, we calculate the normalized area-weighted frequency of positive ice detections and the mean d/D of craters, to find that they are negatively correlated (Fig. 2). We further check and find that this correlation is statistically significant at the 5% significance level (see Supplementary Information).

Data availability

The crater catalogue and data that support the findings of this study are available through figshare with the identifier https://doi.org/10.6084/m9.figshare.7996304. The dataset may also be downloaded from https://figshare.com/s/90fb89d89f35786da658.

Code availability

The code used to model the temperature of permanently shadowed craters[20] can be accessed through a GitHub repository with the identifier https://doi.org/10.5281/

zenodo.3238628. It may also be downloaded from: https://github.com/liorruba/shallow_simple_craters.git.

References

36. Neumann, G. A. *MESSENGER* E/V/H MLA 4 GDR DATA V1.0 (NASA Planetary Data System, 2013).
37. Neumann, G. A. *Lunar Orbiter Laser Altimeter Raw Data Set* LRO-L-LOLA-4-GDR-V1.0 (NASA Planetary Data System, 2010).
38. Bierhaus, E. B. et al. Secondary craters and ejecta across the solar system: populations and effects on impact-crater-based chronologies. *Meteorit. Planet. Sci.* **53**, 638–671 (2018).
39. Schultz, P. H. & Singer, J. A comparison of secondary craters on the Moon, Mercury, and Mars. In *Proceedings Lunar and Planetary Science Conference 11th* 2243–2259 (Pergamon, 1980).
40. Pike, R. J. Apparent depth/apparent diameter relation for lunar craters. In *Proceedings Lunar and Planetary Science Conference 8th* 3427–3436. (Pergamon, 1977).
41. Buhl, D., Welch, W. J. & Rea, D. G. Reradiation and thermal emission from illuminated craters on the lunar surface. *J. Geophys. Res.* **73**, 5281–5295 (1968).
42. Domingue, D. L., Murchie, S. L., Chabot, N. L., Denevi, B. W. & Vilas, F. Mercury's spectrophotometric properties: update from the Mercury Dual Imaging System observations during the third MESSENGER flyby. *Planet. Space Sci.* **59**, 1853–1872 (2011).